Reservoir characterization using crosswell electromagnetic inversion: A feasibility study for the Snorre field, North Sea

G. M. Hoversten*, G. A. Newman[‡], H. F. Morrison*, E. Gasperikova*, and John-Inge Berg**

ABSTRACT

The spatial resolution of a commercially available crosswell electromagnetic (EM) system is demonstrated using models derived from three time steps from a reservoir simulation of the Snorre field in the North Sea. The numerical simulation of the Snorre field waterflood shows that crosswell EM field measurements provide high sensitivity to changes in the reservoir over time. This sensitivity is achieved by combining the reservoir geometry derived from surface 3-D seismic interpretation, reservoir conductivities at well locations, and constrained EM inversion of the reservoir's electrical conductivity.

Inversions of 2-D and 3-D numerical models show that the changes in electrical conductivity attributable to changes in water saturation can be quantitatively mapped as a function of time. The inversions provide smooth estimates of the spatial variation of reservoir electrical conductivity that can discriminate between the level of water saturation at different stages of the waterflood. Inversions performed on 2-D data show that for the Snorre example, 3%–5% Gaussian random noise (depending on the model) can be added without a significant degradation in the inverse models. Two-dimensional inversions of the full 3-D data in the Snorre example can map the vertical average electrical conductivity within the reservoir in the interwell region almost as well as when the model is two dimensional (constant in strike direction). The effect of 3-D structure does not seriously degrade 2-D inversion in the Snorre example—even between wells that lie in a line parallel to structure.

A series of 2-D inversions where various constraints and starting models are used demonstrates the importance of incorporating a priori information in the form of starting models and restricting the inversion domain to the reservoir zone. These tests show that totally unconstrained, smooth inversions of the interwell volume provide very limited quantitative information. However, when the reservoir geometry is constrained by seismic data and starting models are provided by linear interpolation of conductivities at well locations, the reservoir's vertical average electrical conductivity can be predicted to within a few percent by 2-D inversion.

The Snorre field consists of a full-scale reservoir with interwell spacings that exceed 1 km where previous work has demonstrated the applicability of crosswell EM in shallow reservoirs with well separations on the order of 100 m. The simulations show that, given current transmitter and receiver technology, the magnetic fields could be measured in the Snorre field in steel-cased wells separated from the transmitter by up to 725 m.

INTRODUCTION

An essential problem in petroleum production is developing an accurate reservoir description. This description is the basis for reservoir simulation that guides field management, including drilling new wells and designing enhanced recovery processes. Ideally, the simulator provides a 3-D numerical representation of the properties of the reservoir units and the na-ture of their boundaries. In practice, the reservoir engineer may only have the unit boundaries provided by seismic data, limited log data, and in-hole pump tests. Even with data from multiple wells and interference tests, the problem of accurately predicting the properties in the interwell volume can limit the effectiveness of a reservoir model.

Geophysics is playing an increasingly important role in mapping the rock properties between wells and in assigning model

properties in the interwell volume. This is greatly increasing the effectiveness of infill drilling, reservoir production, and reservoir stimulation. Major studies by Lake (1990), Shelton and Cross (1989), and Savit (1987) stress the importance of this new role. Using geophysics to extrapolate borehole data on porosity, saturation, and permeability to the interwell volume and to monitor changes in these reservoir properties over time has revolutionized reservoir engineering.

Methods for inferring porosity based on seismic velocity are now commonly used for inferring interwell variations. Electrical resistivity and sonic logs are currently among the most used well-logging techniques because of their dependence on porosity, saturation, temperature, and clay (shale) content. Electric logs are used routinely to assess saturation, movable oil, and, indirectly, permeability. The reason for this success is that the pore fluid controls the bulk resistivity of most permeable rocks since the current is carried only by ions in solution. Thus, the fractional volume of pore fluid, porosity (ϕ), pore-water resistivity (R_f), water saturation (S_w), and temperature all control the bulk resistivity of the rock, R_b. Traditional well logging estimates the resistivity within a few meters (at most) of the borehole. The crosswell electromagnetic (EM) technique described here is designed to map the resistivity, or its inverse conductivity, between wells at interwell distances up to 1 km.

The basic theory for the use of low-frequency (where displacement currents can be neglected) EM methods for determining R_b between wells on a scale useful for reservoir characterization has been detailed in recent papers and theses. These include Zhou (1989), Spies (1992), Zhou et al. (1993), Alumbaugh et al. (1993), Alumbaugh and Morrison (1993, 1995), Spies and Habashy (1995), and Wilt et al. (1995b). The analyses in general deal with frequencies >1 kHz and where the holes are not cased with steel. In contrasts to these studies, we consider well separations for a full-scale reservoir at a frequency of 50 Hz.

Although we do not include the additional attenuation and phase shifts of steel-cased holes in our analysis, we demonstrate that the attenuation caused by steel-cased wells does not preclude measurements of the magnetic fields in the Snorre example.

SNORRE FIELD

The Snorre field is located on the Tampen spur in the Norwegian sector of the northern North Sea in approximately 300 m of water at depths 2000–2700 m below sea level. The field was discovered in 1979, and production commenced in August 1992. There are two main reservoirs: the Triassic Lunde Formation and the Triassic–Jurassic Statfjord Formation. Each of these reservoirs consists of a network of fluvial sand bodies in a mudstone matrix, deposited in an alluvial setting. As of 1996, there were 20 wells drilled in this field. Two-thirds of these wells produce oil and gas, with the remaining used for water injection. A detailed description of the reservoir characterization of Snorre can be found in Diesen et al. (1995).

Saga Petroleum provided a reservoir simulation of a portion of the field. The simulation covered the area around four existing wells, shown in Figures 1 and 2. Wells P28 and P25 are downdip water injectors, while wells P29 and P18 are updip producers. Figure 2 shows the depth to the top of the reservoir interval, the Statfjord S1 Formation. The total reservoir inter-

val averages 60 m in thickness. The crosswell EM simulations were designed to use well 851, to be drilled as a fiberglass-cased observation well, for the EM transmitters; wells P18, P25, P28, and P29 would be used as EM receiver wells. The cross-section between wells 851 and P28 is essentially perpendicular to strike and is used in a 2-D example. The remaining cross-sections between well 851 and wells P18, P25, and P29 cross the structure at various angles, with the 851–P29 cross-section running essentially parallel to strike. All four well pairs are interpreted using 2-D inversion of the 3-D numerical model magnetic field responses.

The reservoir simulation was done using the GeoQuest Eclipse simulator. Three time snapshots of the reservoir were analyzed. The first time (t_0) represents initial conditions at the beginning of production in August 1992, the second time (t_{140}) represents July 1, 1997, and the third time (t_{160}) represents January 1, 2000. The water saturation values at these times, along with the 3-D seismic top and base of the reservoir, were used with a relationship between water saturation and bulk resistivity derived from log data to produce three 3-D resistivity models of the reservoir zone.

DEPENDENCE OF ELECTRICAL RESISTIVITY ON WATER SATURATION

Figure 3 shows the bulk electrical resistivity (R_b) versus water saturation (S_w) for samples within the reservoir units from wells P18, P28, and P29 at initial conditions. There is a strong correlation between R_b and S_w. The observed data are fit by a linear log–log relation given by equation (1), with a χ^2 misfit of 0.89:

$$R_b = 1.38 * S_w^{-1.7}. \tag{1}$$

This relation is independent of porosity because reduced porosity at Snorre is caused by clay filling the pore space. The increased conductivity of the clay offsets the decrease in resistivity caused by the reduction in pore space.

If the reservoir resistivity can be mapped between wells, there exists the potential of using this relationship for characterizing the reservoir S_w and in monitoring changes in S_w over time as production occurs or as an enhanced recovery process is employed. Ideally, seismic velocity and/or acoustic impedance and resistivity would be mapped as in well logging. Velocity and/or acoustic impedance would then be used to map porosity which, combined with known pore-water resistivities (from the borehole sampling), would then be used to determine S_w from the EM data. It is important to stress, however, that in a given field with known properties at boreholes, the electrical resistivity itself can be used to extrapolate properties between wells even if the process is empirical for that field.

Equation (1) is strictly valid only at initial conditions within the reservoir. Relationships between R_b and S_w depend on whether the reservoir is water wet or oil wet. In particular, Suman and Knight (1997) have studied the behavior of Archie's Law (Archie, 1942) as a function of rock wettability. They conclude that, "Archie's law may be realized only in strongly water-wet systems in which a sufficiently thick water film is present." In addition, they note that wettability has a dominant influence on the relationship between water saturation and bulk resistivity of partially saturated rocks and that oil-wet systems display substantially higher saturation exponent values and significant

hysteresis between drainage and imbibition cycles. Further, the saturation exponent itself can be a function of saturation. This means that additional laboratory work may be required to derive relationships between R_b and S_w that are applicable as waterflooding proceeds in certain reservoirs as a result of the nonlinear relationship between resistivity and saturation changes.

Since we lack the necessary laboratory measurements to improve on equation (1), and since Snorre is a strongly water-wet reservoir, equation (1) should be a good approximation of the true R_b-S_w relationship as waterflooding proceeds. We use equation (1) to convert between R_b and S_w throughout this work. No pore fluid resistivity term is included in equation (1) since the pore fluid resistivity, R_f, is only a few percent different from the resistivity of the injected seawater at reservoir temperatures. Thus, accounting for the mixing of two different-resistivity fluids in the pore volume is not required.

NUMERICAL EM MODEL PARAMETERS

We simulate 3-D EM fields by solving Maxwell's differential equations with a staggered-grid, finite-difference scheme described by Newman (1995). Here, the fields are solved on a grid in the frequency domain for vertical magnetic dipole sources in this application.

In this study, models were run using a background resistivity of 2 ohm-m, representing shale surrounding the reservoir. Vertical magnetic dipole transmitters were simulated in well 851, with receiver locations in the four production wells.
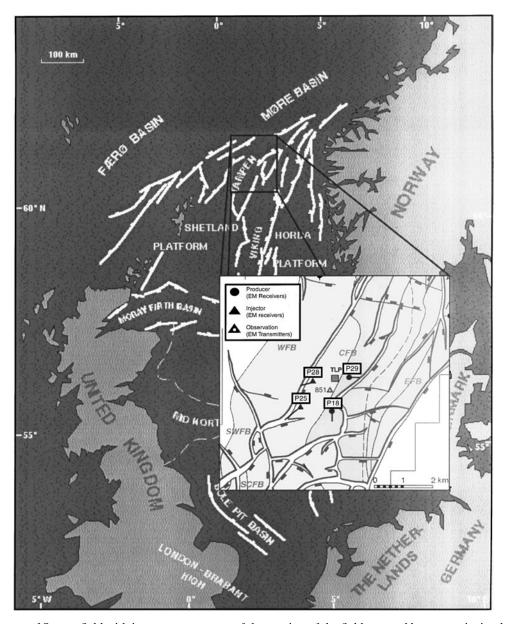

FIG. 1. Location map of Snorre field with inset structure map of the portion of the field covered by reservoir simulation. Wells P25 and P28 are water injectors; wells P18 and P29 are producers; well 851 is a proposed observation well. The numerical simulation of the cross-well EM experiment used well 851 as the transmitter well and wells P18, P25, P28, and P29 as receiver wells.

Transmitters and receivers were located at 10-m intervals from 2320 to 2600 m. Horizontal (radial away from the transmitter) and vertical magnetic fields were calculated at the receiver locations. In these simulations we ignored the effect of steel casing in the wells on the measurements.

The transmitter frequency was chosen to be as high as possible subject to the constraint that the farthest source–receiver separations should not be more than 10 skin depths in the background material. The skin depth is the distance at which the field strength falls off by a factor of $1/e$. The skin depth (δ), in meters, as a function of resistivity (ρ) and frequency (f), is approximately given by

$$\delta \cong 503 \times \sqrt{\frac{\rho}{f}}. \tag{2}$$

The largest source–receiver separations exist between wells 851 and P25. This distance is approximately $10 \times \delta$ at 50 Hz in the 2 ohm-m background.

The 10 skin depth limit was placed on transmitter–receiver separations based on numerical tests of the finite-difference algorithm, comparing results to more numerically stable layered-model algorithms. For homogeneous half-space models when the transmitter–receiver separations became greater than 10 skin depths, the 3-D results began to differ by more than 5% from the correct layered-earth solutions. The resulting limit of 10 skin depths in the numerical models fortunately corresponds with the maximum source–receiver separations achievable in field-data measurements observed by M. J. Wilt (personal communications, 1998).

The choice of mesh parameters such as cell size and overall mesh size are critical for accurate numerical EM modeling. For general inhomogeneous 3-D models such as the Snorre reservoir, the only way to ensure an accurate solution is to first design a mesh that produces solutions that can be checked against accurate 1-D codes. Half-space checks were performed with transmitters located at the top, middle, and bottom of well 851 to all four receiver wells. The maximum difference between 1-D and 3-D solutions was 5%, with an average difference of 2%.
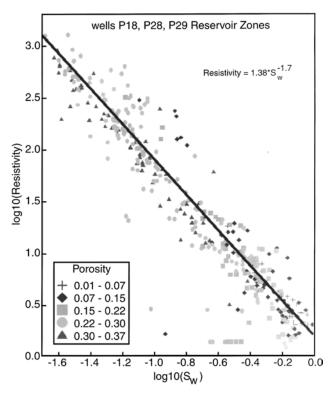

FIG. 3. Resistivity versus water saturation for log samples within the reservoir units from wells P18, P28, and P29. The linear log–log regression fit has $\chi^2 = 0.89$.
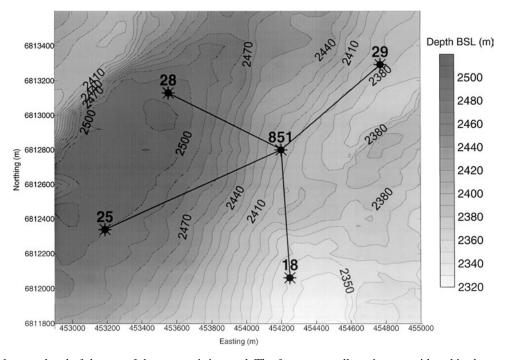

FIG. 2. Depth below sea level of the top of the reservoir interval. The four crosswell sections considered in the study are shown as black lines between observation well 851 and wells P25, P28 (water injectors) and P18, P29 (producers).

Once a 3-D mesh is designed to accurately compute 1-D fields, then the 3-D structure is added and the solutions are compared as the mesh in the region of the 3-D structure is made finer. This is often referred to as a convergence check. Once a stable 3-D solution is reached that does not change as the mesh is made finer, it is deemed correct.

The finite-difference cell sizes in the reservoir zone were $40 \times 40 \times 10$ m in the x-, y-, and z-directions, respectively. Outside the reservoir zone, the cell dimensions were increased to a maximum size of $80 \times 80 \times 20$ m until the mesh boundaries were at least 2 skin depths away from any well in the horizontal directions and 4 skin depths away from any transmitter or receiver in the vertical direction. Total mesh dimensions were $57 \times 50 \times 73$ in the x-, y-, and z-directions, respectively. Models required 285 minutes to run on a 500-MHz DEC Alpha 21264 processor.

PRACTICAL CONSIDERATIONS

For the results to have immediate practical value, we had to consider fields large enough to be measured in the field with existing equipment. The Snorre example represents well separations that range between what is currently possible (7 skin depth separation between wells 851 and P28) and well separations which are just beyond the reach of current technology (10 skin depth separations between wells 851 and P25). Our 2-D study focuses on the cross-section between wells 851 and P28. Our 3-D study will consider all four well pairs with well 851. Although the 851–P25 separation (1.1 km) is not feasible with existing equipment, next-generation transmitters with increased dipole moment will make this possible. Figure 4 shows the vertical and horizontal components of the magnetic field in well P28 for a transmitter above the reservoir in well 851 at initial conditions. This represents a well separation of 725 m.
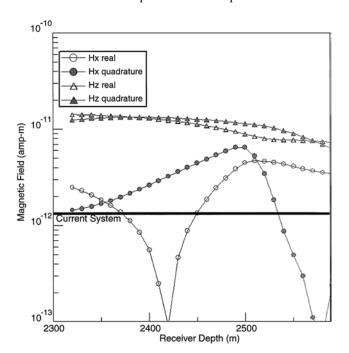

FIG. 4. Vertical (H_z) and radial (H_x) magnetic field components as a function of receiver depth in well P18 for a vertical magnetic dipole transmitter of unit moment at a depth of 2320 m in well 851.

Existing downhole receivers have a noise level amplitude of approximately 4.0×10^{-9} (amp/m)$/\sqrt{H_z}$ at 50 Hz. Assuming 20 s of averaging yields a noise amplitude of

$$\sqrt{(4.0 \times 10^{-9})^2(\text{amp/m})^2/H_z \times (1/20)(H_z)}$$
$$= 8.94 \times 10^{-10}(\text{amp/m}).$$

The vertical magnetic field inside a steel casing embedded in a 2-ohm-m whole space for a transmitter–receiver separation of 725 m was calculated using a code developed by Song and Lee (1998). The casing parameters were outer diameter = 7.5 inches, inner diameter = 6.87 inches, conductivity = 3.6×10^6 S/m, and magnetic permeability = 50 times that of free space. This shows an attenuation of the vertical magnetic field of 0.827 resulting from a single casing at 50 H_z.

The maximum dipole moment of existing downhole vertical magnetic dipole transmitters is 1000 amp-turn-meters. Accounting for a transmitter moment of 1000 and an attenuation factor of $(0.827)^2$ for two casings gives a scaling factor of 684 for the magnetic fields calculated using a unit dipole moment. Thus, for fields for a unit dipole transmitter moment, we can scale the noise amplitude down by 684, yielding a coil noise level of 1.3×10^{-12} (amp-m) per unit transmitter moment, which is shown as Current System on Figure 4.

Since the noise level is inversely proportional to the square root of the bandwidth (the inverse of the averaging period), increasing the averaging time by a factor of 100 will drop the noise level by a factor of 10, assuming a Gaussian noise distribution.

We have performed inversions using either the vertical magnetic field only or using both horizontal (radial from the transmitter) and vertical magnetic fields to demonstrate the differences. However, the horizontal magnetic field sensors in current equipment are approximately 10 times less sensitive than vertical field sensors because of the geometry constraints of operating in the borehole. Thus, with current equipment the vertical magnetic field would be preferred in the Snorre application since acquiring horizontal fields would require additional averaging time. Future systems will be capable of larger dipole moments in the transmitters and more sensitive receivers, making the measurement of horizontal components at the separations present in the Snorre example feasible.

The effect of steel casing is more difficult than the simple attenuation calculation mentioned above would indicate. In addition to the attenuation, large phase shifts are introduced, making it essential that some way of estimating the casing response at each source and/or receiver location be available. One approach is to include a small monitor array in both the transmitter and receiver tools (Lee and Kim, 1998). Algorithms for estimating the casing properties are presented by Wu and Habashy (1994) and Lee and Kim (1998). However, this subject is beyond the scope of this paper. Becker et al. (1998) and downhole EM equipment manufactures are currently working on systems and data-processing techniques to remove the casing response from data prior to inversion.

SENSITIVITY OF VERTICAL MAGNETIC FIELD
TO CHANGES IN S_W

Before considering the quantitative inversion of the crosswell data, it is instructive to look at the changes of the vertical

magnetic field as S_w, and thus R_b, changes. Figures 5 and 6 show the percent changes in the real (in-phase) and quadrature (out-of-phase) components, respectively, of the vertical magnetic fields from t_0 to t_{140} (upper panel) and from t_{140} to t_{160} (lower panel). The percent changes are defined as $((t_{140} - t_0)/t_0) * 100$. The real component at t_0 has a zero crossing, which causes this calculation to become extremely large at certain points. We have therefore removed any value outside the range $\pm 500\%$. This causes the large white area around the central low (Figure 5a). The resistivities of the reservoir zone are shown at the three time steps on the left side of Figure 7.

The largest change is seen in the real component as the reservoir goes from being predominately oil filled with an average S_w near 1% to an average S_w near 10%. A change of over 500% in the real component is seen when the transmitter and receiver are both located in the reservoir zone. The large value of 500% is partially an artifact of the choice of denominator in the percentage calculation since real H_z at t_0 is going through a minimum as the receivers pass through the reservoir. If the

fields at t_{140} are used as the denominator, then the change drops to around 85%. The quadrature changes have no minima and are on the order of 30% to 60% for either choice of denominator in the percent change calculation.

Between t_{140} and t_{160}, the average S_w does not change much but oil is redistributed, causing a decrease of S_w near well 851 (transmitter) and an increase in S_w near well P-28 (receiver). The conductivity increased between 10% and 20% in the bottom portions of the reservoir near the receivers and decreased by as much as 100% in the upper portions of the reservoir near the transmitters. This redistribution of conductivity in the reservoir is reflected in the changes shown in Figure 6. The absolute value of the changes is greatly reduced compared to the changes between t_0 and t_{140}, with maximum changes of 4% and 10% in the real and quadrature components, respectively. Although the changes are smaller, reflecting the smaller changes in reservoir conductivity, the spatial variations are more distinctive, particularly in the quadrature component.
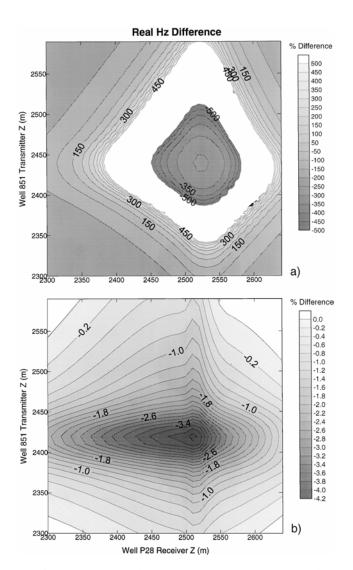

FIG. 5. Percent change in the real component of the vertical magnetic field. (Top) Change between t_0 and t_{140}. (Bottom) Change between t_{140} and t_{160}.
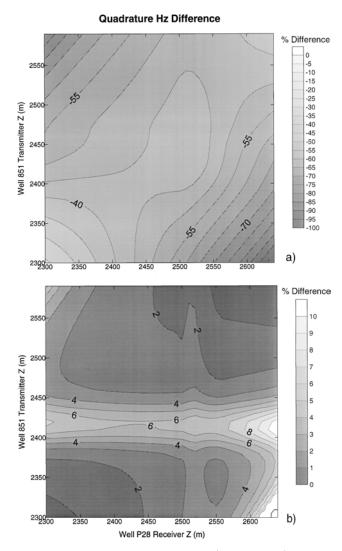
FIG. 6. Percent changes in quadrature (out-of-phase) component of the vertical magnetic field. (Top) Change between t_0 to t_{140}. (Bottom) Change between t_{140} to t_{160}.

INVERSION OF 2-D DATA

Because it is difficult to separate the inherent limitations of 2-D EM inversion from dimensional effects when using a 2-D inversion on 3-D data, a set of 2-D numerical models was generated to represent the cross-section between wells P-28 and 851. We refer to 2-D inversion as a case with a 3-D source and a 2-D structure, sometimes referred to as 2.5-D inversion. Crosswell EM measurements of the real and quadrature vertical magnetic fields can routinely be made with standard deviations of 1% or better at well separations of 6 skin depths in uncased boreholes (M. J. Wilt, personal communication, 1998). The noise level is usually proportional to the total magnetic field. We assume an optimistic 1% noise level; thus, Gaussian random noise with a standard deviation of 1% of the total magnetic field value was added to numerical model data before inversion. In a later section we demonstrate that up to 3% Gaussian random noise does not significantly degrade the t_{140} inversion between wells 851 and P28.

We used a modified version of the inversion algorithm (Appendix) described by Newman (1995). The algorithm uses the starting model as a reference model (σ_0) and solves for perturbation about this reference model. Thus, the inverse parameters are ($\sigma - \sigma_0$). The regularization smoothing is applied to the perturbation ($\sigma - \sigma_0$) rather than to σ itself. The reference model was constructed using 3-D seismic-interpreted top and base reservoir surfaces. The reservoir-zone conductivity was defined at the wells from the logs and linearly interpolated between the wells. The reference model extended the log values without extrapolation to either side away from the wells. The spatial smoothing of the conductivity perturbations was stopped at the reservoir boundaries, allowing a sharp jump in conductivity at these boundaries. Only cells within the reservoir were free to change in the inversion.
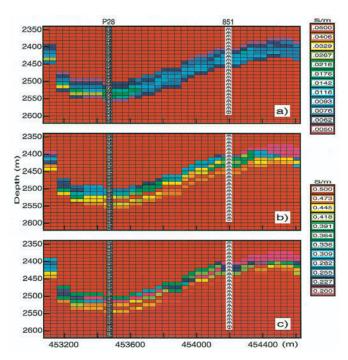
Figure 7 shows the conductivity cross-sections between injector well P28 (left side) and observation well 851 (right side) at the three time steps (t_0, t_{140}, and t_{160}) generated from the reservoir simulation S_w using equation (1). The injector well was used for the EM receivers, and the observation well was used for the vertical magnetic dipole transmitters. Figure 8 shows the inverse model sections at the three reservoir simulation time steps for comparison with the true conductivity sections shown in Figure 7. Only the vertical magnetic field data were used for the inversions shown in Figure 8. All inversions discussed were terminated when the rms data misfit fell below 1. Thus, all data were fit to within the assumed standard errors.

At initial conditions (t_0) when the reservoir is filled mainly with oil and its conductivity is roughly 50 times less than that of the surrounding shale, the radial magnetic field strength at the receivers in the vicinity of the reservoir (the data most sensitive to resolving the reservoir conductivity) is twice that of the vertical magnetic field. At the two later times (t_{140}, t_{160}), the average reservoir conductivity is close to that of the surroundings, and the radial magnetic field is nearly an order of magnitude less than the vertical magnetic field. Since the data errors are assumed to be proportional to the total magnetic field, the S/N ratio of the vertical magnetic field is significantly lower at t_0 than at t_{140} or t_{160}. The reference model constructed from a linear interpolation between the wells of the log conductivities fits the numerical vertical magnetic field data, with 1% total field noise to within an rms error of 1; thus, the model in panel (a) of Figure 8 is the starting model. As will be discussed, when both the vertical and horizontal
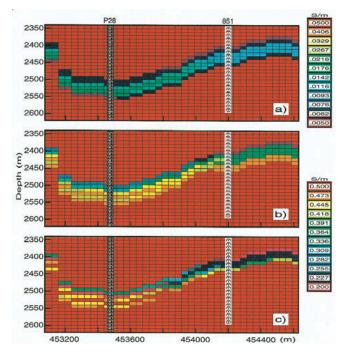

FIG. 7. Reservoir simulations at times t_0, t_{140}, and t_{160}, converted to conductivity using log-derived equation (1).

FIG. 8. Crosswell EM inversions of the numerical data generated from the models shown in Figure 7. The oil buildup is shown in the inversion at t_{160}. The starting model for the reservoir was a linear interpolation of the conductivities at the wells. Water saturation (conductivity) at t_0 is significantly lower than at later times, requiring a change in color tables between t_0 and t_{140}. Inversions for t_{140} and t_{160} are displayed on the same color scale.

fields are used, the inversion can improve on the starting model and more accurately map the interwell conductivity at initial conditions.

PREDICTED WATER SATURATION

To see how the crosswell EM models might provide water saturation estimates to improve reservoir simulations, the inversions in Figure 8 were converted to water saturation using equation (1). Because the reservoir is thin relative to its lateral extent, a useful parameter to summarize its properties is the vertical average conductivity. Profiles between wells P28 and 851 of the true and predicted vertical average conductivity and water saturation within the reservoir are plotted in Figure 9 for the three time steps of the simulation. The scale changes between t_0 and t_{140}. The inversions provide laterally smoothed versions of the true vertical averages.

As stated above, the inversion using only the vertical magnetic field was unable to improve on the starting model in the t_0 case. However, when the reservoir is resistive at t_0, the radial magnetic field has a better S/N ratio (since noise is assumed to be a percentage of the total field) than the vertical field. To demonstrate the improvement in model resolution, inversions for the three time steps were run using both the radial and vertical magnetic fields. The resulting vertical average conductivity profiles are shown in Figure 10. The only important difference in the models comes at t_0, where the inversion is now able to reduce the conductivity in the interwell volume, more closely matching the true distribution. At the later times when the reservoir's average properties are closer to the background values (and the S/N ratio on the vertical component is largest), adding the radial field does not appreciably alter the final models.

Although lateral variations on the scale of 100 m, such as the low in conductivity and S_w between 463 600 and 463 800 at t_{160}, are not reproduced, the inversions provide average properties between the wells that cannot be deduced from well sampling alone. In particular, the inversions show the reduction in conductivity and S_w between the wells at t_0 and the increase in the same region at t_{140} and t_{160}. In addition, the inversions predict the buildup of oil near well 851 at t_{160}, as seen by the decrease in conductivity and S_w between 454 100 and well 851 when the t_{140} and t_{160} predictions are compared.

NOISE

As stated earlier, we have generally assumed an optimistic Gaussian noise level with a standard deviation of 1% of the total magnetic field. To set some limits on what level of noise could be tolerated by the inversions at Snorre and still provide useful interwell conductivity and S_w estimates, we ran the inversions with various noise levels. Figure 11 shows the vertical average conductivity and S_w from three t_{140} models with 1%, 2%, and 3% noise, respectively. At 4% noise the inversion produced an anomalous low conductivity in the interwell region. The inversions with up to 3% noise show only small differences from one another but in general tend to reduce the estimate of the anomalous high conductivity in the interwell region as the noise increases. Inversions for t_{160} were very similar to t_{140}, and the t_0 inversions were able to tolerate 5% noise before losing the ability to predict the decrease in interwell conductivity. These tests indicate that for the Snorre example the maximum tolerable noise level is 3%–5%.
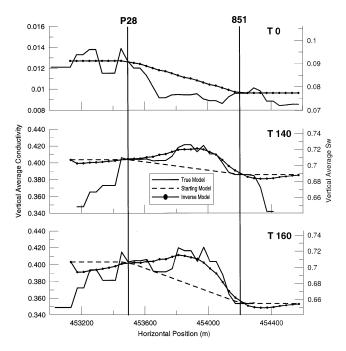

FIG. 9. Comparison of vertically averaged conductivity and water saturation within the reservoir and that estimated from the crosswell inversions of numerical vertical magnetic field data. Well P28 is located at 453 474 m; well 851 is located at 454 200 m. (Top) Initial conditions. (Middle) Reservoir at t_{140}. (Bottom) Reservoir at t_{160}.
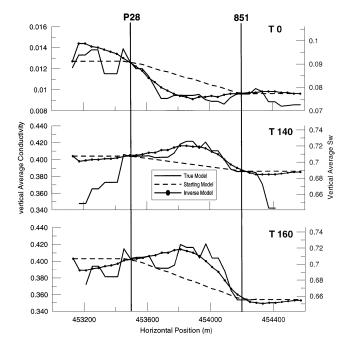

FIG. 10. Comparison of vertically averaged conductivity and water saturation within the reservoir and that estimated from the crosswell inversions of numerical vertical and radial magnetic field data. Well P28 is located at a distance of 453 474 m; well 851 is located at 454 200 m. (Top) Initial conditions. (Middle) Reservoir at t_{140}. (Bottom) Reservoir at t_{160}.

EFFECTS OF CONSTRAINTS AND A PRIORI INFORMATION

The 2-D inversions of 2-D data previously discussed have used (1) structural information from surface seismic data to constrain the inversion domain to the reservoir and (2) log conductivity data to provide a smooth reference model for inversion. It is important to understand the contributions of structural constraints and a priori information on the spatial resolution of crosswell EM data. To this end we generated four inversions of the t_{140} vertical magnetic field data with 1% noise. Figure 12 shows these inversions; the true conductivity section and the fully constrained inversion are shown in Figures 7b and 8b, respectively. The vertical average conductivities within the reservoir for the four inversions, along with the true model and fully constrained inversion, are plotted in Figure 13.

Figure 12a shows the t_{140} inverse model when no structural constraints or a priori information is used. The starting model for the inversion was a half-space of 0.5 S/m, representing the surrounding shale. While the inverse model does show the correct reservoir geometry between the wells, the spatial smoothing [the regularization term $(W(\sigma - \sigma_0))(W(\sigma - \sigma_0))^T$ in equation (A-6) of the Appendix] has spread the conductivity distribution over a much larger area than the reservoir, resulting in little detail within the reservoir zone itself. The vertical average conductivity shown in Figure 13 qualitatively indicates the increased conductivity in the interwell region, but the entire curve is biased upward by its connection (through smoothing) to the 0.5-S/m material of the starting model outside of the inversion domain.

Figure 12b shows the t_{140} inverse, again starting with a 0.5-S/m half-space, where the inversion domain is limited to the reservoir. In this case smoothing across the reservoir boundaries is still enforced, causing a smooth gradation from the surrounding 0.5 S/m to the less conductive material in the center of the reservoir. The vertical average conductivity (Figure 13) again indicates increased conductivity in the interwell region but varies
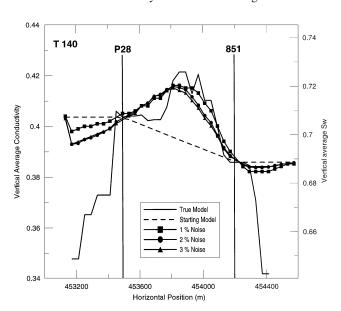

FIG. 12. Four inversions of the 2-D t_{140} vertical magnetic field data with 1% noise. (a) Starting model was 0.5 S/m half-space with no constraints. (b) Starting model was 0.5 S/m half-space; inversion domain was confined to the reservoir zone. (c) Starting model was 0.5 S/m half-space; inversion domain was confined to the reservoir zone, and model smoothing stopped at the reservoir boundaries. (d) Starting model was linearly interpolated well-log conductivities, with no breaks in model smoothing, and the entire cross-section was free to change in the inversion.

FIG. 11. Effects of noise levels on t_{140} inversion of 2-D data. As the noise level increases, the estimated conductivity in the interwell region decreases. Beyond 3% random Gaussian noise, the inversion does not predict the increase in interwell conductivity.
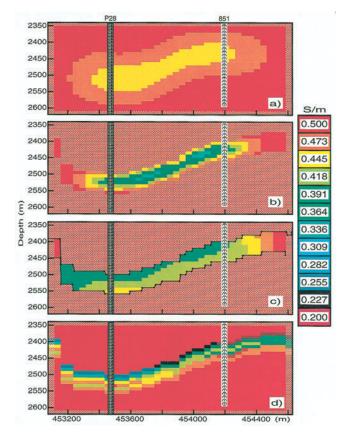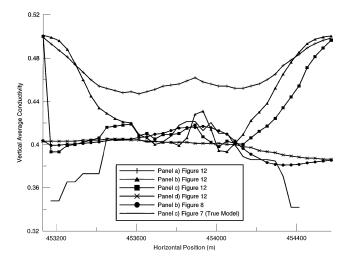

FIG. 13. Vertical averaged conductivity from the four inverse models shown in Figure 12 and the fully constrained inverse shown in Figure 8, along with the true values from the model in Figure 7b.

sharply laterally and swings up to the 0.5 S/m of the starting model on either end of the inversion domain.

Figure 12c shows the inverse model when the smoothing across the reservoir boundaries is eliminated. This allows the conductivity to jump across these boundaries. The starting model is still a 0.5-S/m half-space. The impact of eliminating smoothing across boundaries in the model can be seen by comparing the conductivity estimates at the left end (453 100) of the sections for Figures 12b and 12c. In the inversion in Figure 12b, the conductivity smoothly varies up to the edge value of 0.5 S/m. In the inversion in Figure 12c, the break in smoothing which coincides with the vertical fault in the reservoir at 453 100 m allows the conductivity to remain low up to the fault. In this example the inversion indicates (1) the increased conductivity in the interwell region and (2) the correct vertical variation in conductivity within the reservoir (less conductive at the top, more conductive at the bottom). This is significant because it indicates sensitivity to vertical conductivity variations within the reservoir.

Finally, Figure 12d shows the inverse where the starting model is the linearly interpolated well conductivities but where no constraints have been placed on the inversion domain and where the smoothing of the model perturbations exists across the reservoir boundaries. In this case very small changes have been made to the surrounding conductive material outside of the reservoir to accommodate the data. These changes (on the order of 5% to 10%) do not show up on this color scale but are enough to fit the data while the vertical average conductivity within the reservoir changes little from the starting values.

These examples highlight the limitations of the crosswell EM technique when used without a priori information. It also demonstrates the significant improvement in spatial resolution of the vertically averaged reservoir conductivity (and thus the implied S_w) that can be achieved when both structural information from seismic data and a priori conductivity information from logs are incorporated. The case shown in Figure 12c, with the vertical fault at 453 100, also indicates the potential improvement in lateral resolution in the interwell region if seismic data could be used to locate faults.

2-D INVERSION OF 3-D DATA

The vertical magnetic field response from the 3-D numerical model at t_{140} was inverted using the 2-D algorithm previously described. Four well pairs were considered: (P28, 851), (P29, 851), (P25, 851), and (P18, 851). The 2-D inversions all used starting and reference models constructed by linear interpolation of the well conductivities. Perturbations about the reference model within the reservoir zone were solved with the smoothing eliminated across the reservoir boundaries. Figure 14 shows the vertical average conductivity for the four inverse models.

The section between wells P28 and 851 (Figure 2) is essentially perpendicular to the local structure. The 3-D and 2-D vertical magnetic fields differ by <5% at the extreme transmitter–receiver separations. As would be expected, the 2-D inverse of the 3-D data predicts the interwell conductive as well as in the purely 2-D case. At the other extreme is the section between wells P29 and 851, which is almost parallel to the local structure. This section, which should show the largest departure from a 2-D response, is fairly well modeled by the 2-D

inversion. Figure 15 compares between 2-D and 3-D real and quadrature vertical magnetic fields for this section. The real components differ by a maximum of 3.5% when both the transmitter and receivers are within the reservoir. The quadrature component also differs by approximately 3.5% when the transmitter and receivers are within the reservoir. A maximum difference in the quadrature component of 40% occurs for the extreme transmitter–receiver separations. However, these large differences occur at only a few data points in the quadrature component.

To understand the spatial distribution of model sensitivity, we have computed the 3-D Jacobian or sensitivity matrix for the 3-D model at t_{140}. Rather than use the integral equation solution for the sensitivity matrix from infinitesimal volumes in a whole space as done by Spies and Habashy (1995), we have used the adjoint method for the 3-D finite-difference solution [Newman and Alumbaugh (1997)]. The sensitivities were calculated for each cell in the 3-D model (cell sizes $40 \times 40 \times 10$ m) and normalized to the maximum value. Values of the normalized $\log_{10}$ real vertical magnetic-field sensitivity for a transmitter and receiver located within the reservoir at a depth of 2400 m were contoured and overlain on color contours of the vertical average reservoir conductivity (Figure 16). The -1 and -2 contours represent 1/10 and 1/100 of the maximum sensitivity, respectively. Figure 16 shows that the sensitivity drops to 1/10 of the maximum for cells only 100 m off-line between the wells. In addition, the distorting effects the variable conductivity distribution can be seen in the sensitivity pattern. In the interwell region the 0.5 contour encompasses a larger region farther away from well P29 compared with well 851 because of the decrease in conductivity near well P29. All sensitivity contours are moved farther away from the wells in the less conductive areas compared with the more conductive areas. As a result of the asymmetry of the conductivity distribution,
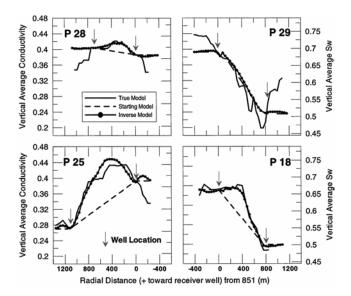

FIG. 14. Vertical averaged conductivity and estimated S_w for the four crosswell sections shown in Figure 2. These were generated from 2-D inversion of 3-D vertical magnetic field data with 1% noise level. (Upper left) Section between wells 851 and P28. (Upper right) Section between wells 851 and P29. (Lower left) Section between wells 851 and P25. (Lower right) Section between wells 851 and P18.

cells 150 m to the northwest in the more conductive material have only 1/100 the maximum sensitivity. To the southeast, in less conductive material, the 1/100 value is not reached until 200 m offline.

The ability to reconstruct the vertical average reservoir conductivity between wells in this 3-D geometry using 2-D inversion is better than might be indicated by considering uniform whole-space sensitivities. Spies and Habashy (1995) conclude that the strike length of a feature would have to be approximately equal to the source–receiver separation to appear two dimensional. While true, this statement does not mean that 3-D geology must meet this criteria for 2-D inversion to be useful. In our example considerable conductivity variation occurs out of the plane of the transmitter and receiver wells within distances a fraction of the well separation. The ability to constrain the inversion domain to the reservoir zone and use a reference model generated from the log conductivity at the wells greatly improves the ability to predict the average reservoir conductivity between the wells. In general, at least for the Snorre example, 2-D inversion of 3-D data does a good job of representing the smoothed vertically averaged interwell reservoir conductivity.

DISCUSSION

This study is a beginning. The crosswell EM technique has the ability to map conductivity and, hence, infer water saturation in the interwell volume on a scale that can provide useful updates for reservoir simulations. The maximum benefit from the technique will be derived when it is used in conjunction with both seismic data and production history, matching by reservoir simulation. In the example presented here, seismic data were essential to provide the reservoir geometry. This greatly constrains the volume available for the EM inversion to update and thus greatly reduces problems of nonuniqueness. Additional data sets will provide more detailed starting models (reference models) for the EM inversions. We see the process as iterative, in which the models (reservoir simulation, seismic velocity, and electrical conductivity) feed back to one another until all data are satisfied with a self-consistent rock properties model. That is, the porosity, water saturation, velocity, and resistivity can all be explained by one set of empirical relations that match observed well-log and laboratory data. In this example where no interwell information was built into the reference model, the linear interpolation of log values provided a smooth reference model. When additional information, from either reservoir simulation models or seismic data, is used to provide reference models with more internal structure, crosswell EM inversion can be used to solve for perturbations about these more detailed models which satisfy the EM data.

A significant benefit will be derived when either crosswell seismic and/or surface seismic data are used to estimate interwell porosity. In many situations the pore fluid will be considerably more conductive than the injected water. In these cases the porosity will become an additional parameter since an accurate bulk resistivity estimate will require mixing the two different fluid resistivities within the pore space.

We intend to continue working on this and other examples by extending the inversion work to three dimensions. Working in three dimensions increases the computational load significantly but is still possible on current high-end workstations. For
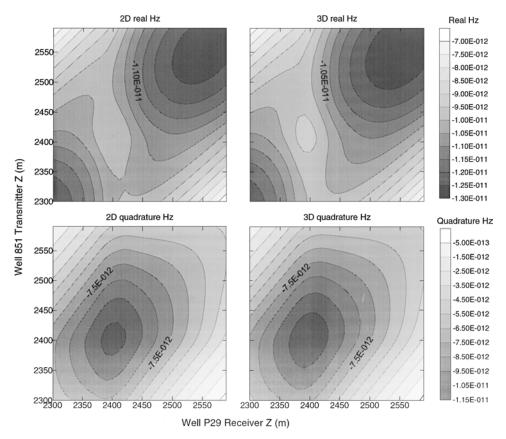

FIG. 15. Comparison between 2-D and 3-D vertical magnetic fields calculated for transmitters in well 851 and receivers in well P29. This crosswell section is essentially parallel to local geologic strike.
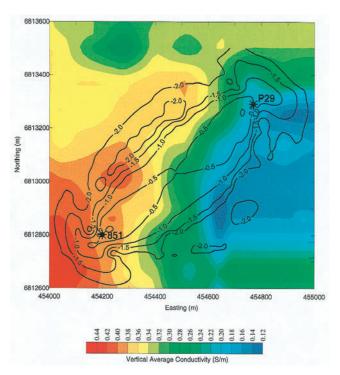
FIG. 16. Vertical averaged conductivity within the reservoir at t_{140}, shown in color contours. The 3-D sensitivity (values of the Jacobian matrix) for a transmitter and receiver at a depth of 2400 m (within the reservoir) are shown as black contour lines. The sensitivities are in $\log_{10}$ of the normalized absolute value. Contour values of -1 and -2 represent 1/10 and 1/100 of the maximum sensitivity, respectively.

larger scale 3-D inversion applications, massively parallel computing platforms can be used (see Newman and Alumbaugh, 1997).

CONCLUSIONS

The forward modeling of the Snorre reservoir waterflood has demonstrated two important facts that make the technique feasible for field use. First, a commercially available system could produce measurable magnetic fields for the Snorre environment. Second, the observed vertical magnetic fields bear a strong qualitative relation to changes in the reservoir as waterflooding proceeds.

Two-dimensional inversions of crosswell EM data can provide quantitative predictions of the vertical average reservoir conductivity at different time steps of a petroleum reservoir waterflood. In addition, provided that relations between conductivity and S_w can be determined, they can also quantitatively predict water saturation in the interwell region. Two-dimensional inversions of fully 3-D data for the Snorre example predict the vertically averaged reservoir conductivity almost as accurately as in the purely 2-D example. This demonstrates that 2-D inversion of crosswell EM data can provide useful information in realistic 3-D petroleum reservoirs.

The ability to constrain crosswell EM inversions by incorporating reservoir structure from surface seismic data as well as provide reference models based on interpolated log conductivity greatly improves our ability to quantitatively map average reservoir conductivity. Without these constraints crosswell EM

can map gross structural features and provide qualitative estimates of relative high- and low-conductivity zones in the interwell region but cannot predict conductivity accurately enough to be used in estimates of water saturation.

REFERENCES

Alumbaugh, D. L., and Morrison, H. F., 1993, Electromagnetic conductivity imaging with an iterative Born inversion: IEEE Trans. Geosci. Remote Sensing, **31**, 758–763.
——— 1995, Theoretical and practical considerations for crosswell electromagnetic tomography assuming a cylindrical geometry: Geophysics, **60**, 846–870.
Alumbaugh, D. L., Becker, A., Morrison, H. F., Lee, K. H., and Wilt, M. J., 1993, Saltwater injection monitoring with cross-hole EM: A report of 1992 field activities at the UC Richmond field station: Lawrence Berkeley Nat.'l Lab. Rpt. LBL-33000.
Archie, G. E., 1942, The electrical resistivity log as an aid in determining some reservoir characteristics: Trans. AIME, **146**, 54–61.
Becker, A., Wang, B., Lee, K. H., and Wilt, M., 1998, Subsurface electromagnetic measurement through steel casing: Lawrence Berkeley Nat.'l Lab. Rpt. LBNL-42375.
Diesen, G. W., Edvardsen, A., Nystuen, J. P., and Tollefsrud, J. I., 1995, Geophysical and geological tools and methods used for reservoir characterization and modelling of the Snorre field—North Sea, Norway: Techn. Research Centre, Special Publication JNOC, **5**, 69–90.
Fletcher, R., and Jackson, M. P., 1974, Minimization of a quadratic function of many variables subject only to lower and upper bounds: J. Inst. Math. Appl., **14**, 159–174.
Lake, L. W., 1990, What engineers need for numerical simulation: Internat. Symp. on Borehole Geophys., Univ. of Arizona and Soc. Expl. Geophys.,
Lee, K. H., and Kim, H. J., 1998, Electromagnetic method for analyzing the property of steel casing: Lawrence Berkeley Nat.'l Lab. Rpt. LBNL-41525.
Newman, G. A., 1995, Crosswell electromagnetic inversion using integral and differential equations: Geophysics, **60**, 899–911.
Newman, G. A., and Alumbaugh, D. L., 1997, Three-dimensional massively parallel electromagnetic inversion—I: Theory: Geophys. J. Internat., **128**, 345–354.
Savit, C., 1987, New ways to study the earth: CONF-8705179, Research needs for hydrocarbon fuels, U.S. DOE, Workshop Report, 16–18.
Shelton, J. L., and Cross, T. A., 1989, The influence of stratigraphy in reservoir simulation, *in* Quantitative dynamic stratigraphy: Prentice-Hall, Inc., 589–600.
Song, Y., and Lee, Ki Ha, 1998, Electromagnetic fields due to a loop current in a cased borehole surrounded by uniform whole space: Lawrence Berkeley Nat.'l Lab. Rpt. LBNL-42371.
Spies, B. R., 1992, Survey design for cross-well electromagnetics: 62nd Ann. Internat. Mtg., Soc. Expl. Geophys., Expanded Abstracts, 498–501.
Spies, B. R., and Habashy, T. M., 1995, Sensitivity analysis of cross-well electromagnetics: Geophysics, **60**, 834–845.
Suman, R. J., and Knight, R. J., 1997, Effects of pore structure and wettability on the electrical resistivity of partially saturated rocks—A network study: Geophysics, **62**, 1151–1162.
Tikhonov, A. N., and Arsenin, V. Y., 1977, Solutions to ill-posed problems: John Wiley and Sons, Inc.
Wang, T., and Hohmann, G. W., 1993, A finite difference time-domain solution for three-dimensional electromagnetic modeling: Geophysics, **58**, 797–809.
Wilt, M. J., Alumbaugh, D. L., Morrison, H. F., Becker, A., Lee, K. H., and Dezcz-Pan, M., 1995a, Crosshole electromagnetic tomography: Design considerations and field results: Geophysics, **60**, 871–885.

Wilt, M. J., Morrison, H. F., Becker, A., Tseng, H. W., Lee, K. H., Torres-Verdin, C., and Alumbaugh, D. L., 1995b, Crosshole electromagnetic tomography: A new technology for oil field characterization: The Leading Edge, **14**, 173–177.

Wu, X., and Habashy, T. M., 1994, Influence of steel casings on electromagnetic signals: Geophysics, **59**, 378–390.

Zhou, Q., 1989, Audio-frequency electromagnetic tomography for reservoir evaluation: Lawrence Berkeley Nat.'l Lab. Rpt. LBL-28171.

Zhou, Q., Becker, A., and Morrison, H. F., 1993, Audio-frequency electromagnetic tomography in 2-D: Geophysics, **58**, 482–495.

APPENDIX

INVERSE MODELING

Given a 3-D conductivity distribution in the earth, $\sigma(r)$, the EM fields, neglecting displacement currents, can be described by the integral equation

$$\mathbf{d^{Fp}}(\mathbf{r}) = \mathbf{d^{F(i)}}(\mathbf{r}) + \int_v \mathbf{G^{F(i)}}(\mathbf{r}, \mathbf{r'})\mathbf{E}(\mathbf{r'})\big(\sigma(\mathbf{r}) - \sigma^{(i)}(\mathbf{r})\big)\, dv', \tag{A-1}$$

where $\mathbf{d^{Fp}}$ is the computed electric or magnetic field, $\mathbf{d^{F(i)}}$ is the background electric or magnetic field, and $\mathbf{G^{F(i)}}(\mathbf{r}, \mathbf{r'})$ is the electric or magnetic field tensor Green's function. Since E is also a function of $\sigma(\mathbf{r})$, equation (A-1) is nonlinear in σ. The superscript i refers to some background model, and $\mathbf{E}(\mathbf{r'})$ is the internal electric field. This background model, its fields, and the Green's functions are not required to be one dimensional and are assumed to be known. However, the internal electric field $\mathbf{E}(\mathbf{r'})$ is unknown.

Equation (A-1) can be written in discrete form, specialized for 2-D crosswell configurations. The integration over the volume is replaced by two summations over N_{xz} cells in the crosswell (x–z) plane and over N_y cells along the y-axis or strike direction. Specifically,

$$\mathbf{d^{Fp}}(\mathbf{r_k}) = \mathbf{d^{F(i)}}(\mathbf{r_k}) + \sum_1^{N_{xz}} \big(\sigma(\mathbf{r_n}) - \sigma^{(i)}(\mathbf{r_n})\big)$$

$$\bullet \sum_1^{N_y} \underset{\sim}{\mathbf{\Gamma}}^{\mathbf{F(i)}}(\mathbf{r_k}, \mathbf{r_{n,j}})\mathbf{E}(\mathbf{r_{n,j}}), \tag{A-2}$$

where the tensor Green's function for a prism of current with its center at $r_{n,j}$ is defined as

$$\mathbf{\Gamma^{F(i)}}(\mathbf{r_k}, \mathbf{r_{n,j}}) = \int_{vnj} \mathbf{G^{F(i)}}(\mathbf{r_k}, \mathbf{r'})\, dv'. \tag{A-3}$$

Because the conductivity in equation (A-2) does not depend on the index j but only on n, it is a 2-D distribution.

The major difficulty in using equation (A-2) to obtain estimates of $\sigma(\mathbf{r_n})$ is that it is nonlinear in $\sigma(\mathbf{r_n})$. Equation (A-2) can be linearized using the Born approximation, where the electric field is that of the background. Thus, under the Born approximation equation (A-2) is written as

$$\mathbf{d^{Fp}}(\mathbf{r_k}) = \mathbf{d^{F(i)}}(\mathbf{r_k}) + \sum_1^{N_{xz}} \mathbf{A_{k,n}^{F(i)}}\big(\sigma(\mathbf{r_n}) - \sigma^{(i)}(\mathbf{r_n})\big), \tag{A-4}$$

where

$$\mathbf{A_{k,n}^{F(i)}} = \sum_{j=1}^{N_y} \underset{\sim}{\mathbf{\Gamma}}^{\mathbf{F(i)}}(\mathbf{r_k}, \mathbf{r_{n,j}})\mathbf{E}^{(i)}(\mathbf{r_{n,j}}). \tag{A-5}$$

Regularized least squares

Because the inverse problem is underdetermined, it is unstable and ill posed. Reliable estimates of $\sigma(\mathbf{r_n})$ may be possible if equation (A-4) is stabilized in a least-squares sense with regularization (Tikhonov and Arsenin, 1977). Regularization removes solutions that are too rough by adding a model roughness term to the object function being minimized. Reconstructions are required to be smoothed versions of the earth's electrical properties at the expense of an increase in the fitting error.

The following functional can provide smooth reconstructions if it is minimized with respect to the model parameters $\sigma(\mathbf{r_n})$ subject to inequality constraints:

$$S = \lambda^{-1}\Big\lfloor \big(\mathbf{D}\big(\mathbf{d^F} - \mathbf{d^{F(i)}} - \mathbf{A^{F(i)}}\big(\sigma - \sigma^{(i)}\big)\big)\big)^{\mathrm{T}}$$

$$\times \big(\mathbf{D}\big(\mathbf{d^F} - \mathbf{d^{F(i)}} - \mathbf{A^{F(i)}}\big(\sigma - \sigma^{(i)}\big)\big)\big) - \chi^2 \Big\rfloor$$

$$+ \beta(\mathbf{W}(\sigma - \sigma_0))^{\mathrm{T}}(\mathbf{W}(\sigma - \sigma_0)). \tag{A-6}$$

Here we minimize model roughness $(\mathbf{W}(\sigma - \sigma_0))^{\mathrm{T}}(\mathbf{W}(\sigma - \sigma_0))$ subject to a specified squared error χ^2. The superscript T denotes the transpose operator. The matrix $\mathbf{W}$ is the roughness matrix, consisting of a finite-difference approximation to the Laplacian (∇^2) operator. In equation (A-6) the vector $\mathbf{d^F}$ is the observed data. The data weighting matrix $\mathbf{D}$ can take many forms; however, in our case it is diagonal and contains the reciprocal of the data standard deviations. The last term in equation (A-6) is added to solve for perturbations about some reference model σ_0.

The parameter λ is the trade-off between model smoothness and data fit. Its selection requires special care if the inverse solution is to provide acceptable results. There is no universal or unique strategy for selecting λ in equation (A-6). It is important, however, to select it such that there is an acceptable trade-off between model smoothness and data fit. Selecting trade-off parameters that are too small can produce models that are physically unreasonable in that the models are spatially too rough but can produce superior data fits. Trade-off parameters that are too large produce highly smoothed models, but these models show poor dependence of the data.

Because equation (A-6) is a quadratic functional, its minimization subject to inequality constraints is a linear programming problem. The solution to this problem can be found using the algorithm of Fletcher and Jackson (1974). Inequality constraints are incorporated into the inverse problem to omit solutions that are not reasonable given prior information.

The inversion algorithm was modified to fix cell resistivities outside the reservoir and to place tears in the smoothing matrix. This enabled us only to invert for a smooth conductivity distribution within the reservoir zone. The boundaries of the reservoir were defined by surface 3-D seismic data. These boundaries were used to place tears in the smoothing matrix so the inverse model did not smooth resistivities across the top and base of the reservoir.